AR-Aided Smart Sensing for In-Line Condition Monitoring of IGBT Wafer

Kongjing Li, *Member, IEEE*, Gui Yun Tian, *Senior Member, IEEE*, Xiaotian Chen, Chaoqing Tang, Haoze Luo, *Member, IEEE*, Wuhua Li, *Member, IEEE*, Bin Gao, *Senior Member, IEEE*, Xiangning He, *Fellow, IEEE*, and Nick Wright

***Abstract*—This paper describes an augmented reality (AR)-aided smart sensing technique for in-line condition monitoring of insulated-gate bipolar transistor (IGBT) wafers. A series of signal processing algorithms are applied for enabling sensor intelligence. Based on electromagnetic infrared–visible fusion (IVF), a supplementary palpable three-dimensional thermography layer is integrated with an IGBT wafer in real world environment. Before the IVF, independent component analysis is implemented to identify defects in the wafer. The proposed AR-aided smart sensing technique enhances user's perception and interaction between the industrial systems and the surrounding world. In contrast to conventional sensor techniques, it provides nondestructive testing and evaluation based high-throughput in-line condition monitoring method. The advantages of noncontact and time efficient of this smart sensing technique potentially bring huge benefit to yield management and production efficiency. AR-aided smart sensing can improve the productivity, quality, and reliability of power electronic materials and devices, as well as in other industrial applications.**

***Index Terms*—Augmented reality (AR), eddy current pulsed thermography, IGBT, nondestructive testing, smart sensing, wafers.**

I. Introduction

AS THE core element of power electronic devices, the quality of insulated-gate bipolar transistor (IGBT) dies is crucial for the reliability and life cycle of the power electronic systems [1]–[3]. With the rapid development of more electric human transport applications, such as more electric airplane and consumer hybrid/pure electric vehicles, the standards of quality and reliability of power electronic dies have been raised to an unprecedented level [4]. However, due to the weak global economy, governments pull back on spending in areas such as public transportations and renewable energies [5], [6]. This fiscal austerity makes IGBT producers meet the challenges of improving performance, quality, and reliability of the products, while simultaneously meeting the pressures of increasing cost for renewing industrial equipment along with fewer government contracts and grants [7]. Based on current process and techniques of IGBT wafer manufacturing, one of the best options for manufacturers is to reduce defects that affect yield in the fabrication facilities, or fabs is to apply higher performance sensor systems [8]–[11]. With the new control strategies and higher precisions, better resolutions of the electrical parameters of the product wafer can be obtained with the sensor systems. However, they cannot provide any physical information of the defects; it is hard to evaluate the types of defects, which affected the electrical performance of the semiconductor dies. The final stage of IGBT wafer fabrication is the quality inspection, which is before assembly and packaging to power devices. The product wafer contains an array of identical circuits called dies. Sensors are employed to scan and test each die to confirm that they are fully functional and free defects. Any unqualified die would be rejected and marked with a black ink dot in the middle of the surface. Before getting into the further assembling stage, these defective dies should be discarded after dicing. Unfortunately, the productivity of fabs is strongly limited by current sensing technologies for IGBT wafers. In other words, the sensing technology is the bottleneck of the productivity in IGBT industry. It is urgent to develop a smart sensor system to release the throughput capability of other manufacturing stages in the industry.

Currently, two main categories of the sensor are employed for inspection and testing of IGBT wafers, respectively. The first category is the optical-sensor-based microscopy technology employed for inspecting the surface contamination on wafers [12]–[15]. There are two typical systems for contamination detection under this category that are optical imaging inspection in both bright-field (BF) and dark-field (DF) modes, and optical scattering scanning in the DF mode. In essence, the BF mode evaluates the specular beam of the incident light, which is reflected by the wafer surface, and the DF mode evaluates

Manuscript received November 21, 2017; revised May 5, 2018, July 13, 2018, and October 10, 2018; accepted November 22, 2018. Date of publication January 1, 2019; date of current version May 31, 2019. This work was supported in part by the U.K. EPSRC under Grant EP/J012343/1 and in part by the China NSFC under Grant 6152780147. *(Corresponding author: Gui Yun Tian.)*

K. Li, X. Chen, C. Tang, and N. Wright are with the School of Engineering, Newcastle University, NE1 7RU Newcastle upon Tyne, U.K. (e-mail: k.li3@ncl.ac.uk; c.xiaotian1@newcastle.ac.uk; c.tang2@newcastle.ac.uk; nick.wright@newcastle.ac.uk).

G. Y. Tian is with the School of Engineering, Newcastle University, NE1 7RU Newcastle upon Tyne U.K. and also with the School of Automation Engineering, University of Electronic Science and Technology of China, Chengdu 611731, China (e-mail: g.y.tian@uestc.edu.cn).

H. Luo, W. Li, and X. He are with the College of Electrical Engineering, Zhejiang University, Hangzhou 310027, China (e-mail: luohaoze@163.com; woohualee@zju.edu.cn; hxn@zju.edu.cn).

B. Gao is with the School of Automation Engineering, University of Electronic Science and Technology of China, Chengdu 611731, China (e-mail: bin_gao@uestc.edu.cn).

Color versions of one or more of the figures in this paper are available online at http://ieeexplore.ieee.org.

Digital Object Identifier 10.1109/TIE.2018.2886775

0278-0046 © 2018 IEEE. Translations and content mining are permitted for academic research only. Personal use is also permitted, but republication/redistribution requires IEEE permission. See http://www.ieee.org/publications_standards/publications/rights/index.html for more information.

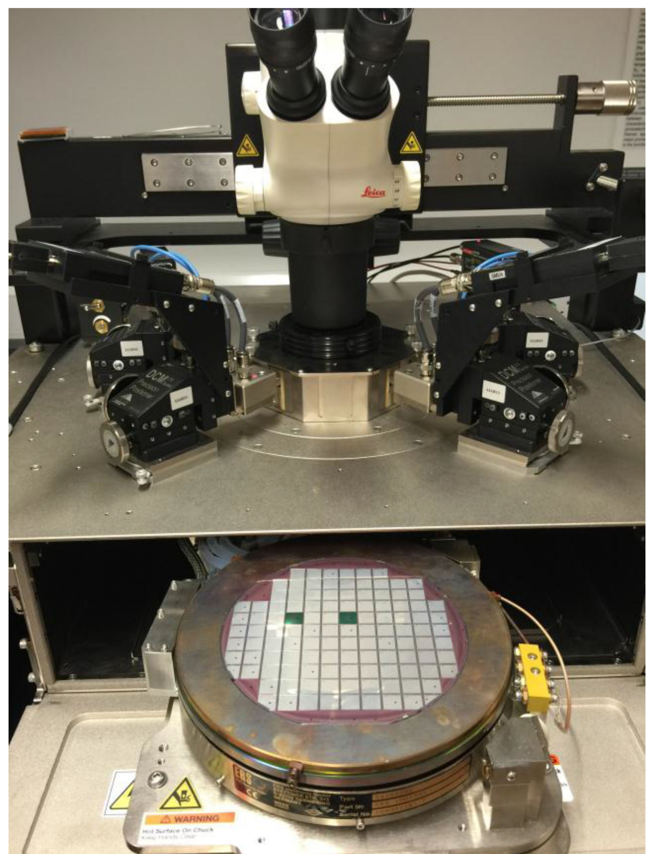

Fig. 1. IGBT wafer on test rig prepares for electrical probing.

scattered illumination/laser, which is the light scattered to areas outside the specular beam due to material properties and defects topographies. In the optical inspection, a defect can be detected on one die under test (DUT) by comparing it to its neighbors. Any abnormal features would be extracted and become candidates for defects review in the later process. The second sensor category is electrical-based probing technology for testing the electrical parameters of product wafers [16]–[21].

The advantage of probing method is to measure multiple electrical parameters of each die in high sensitivity; however, the testing efficiency is low. For a modern 6-in IGBT wafer, the test procedure normally costs at least 1-2 h; multiple probing cards are required to increase testing efficiency, but this would have resulted in much higher cost. Since the DUT is IGBT, it requires the sensors to delivery and suffers from high voltage and high current for evaluating the electrical performance of the DUTs. The electrical parameters of power device include two categories, static characteristics (SCs) and dynamic characteristics (DCs). Fig. 1 shows an IGBT wafer prepared for conducting SC testing. SCs include three voltage parameters ($V_{\rm (BR)CES}$, $V_{\rm CE(ON)}$/$V_{\rm CEsat}$, and $V_{\rm GE(th)}$), and two leakage current parameters ($I_{\rm CES}$ and $I_{\rm GES}$). Unqualified $V_{\rm (BR)CES}$ and $V_{\rm GE(th)}$ provide information of doping defects during the manufacturing process. Unqualified $V_{\rm CE(ON)}$/$V_{\rm CEsat}$, $I_{\rm CES}$, and $I_{\rm GES}$ are important indicators of any mechanical defects inside of the IGBT dies [22], [23]. Compared to SCs, DCs are more attractive to both manufacturers and end consumers since they can simulate the dynamic switching behaviors in intricate working conditions of realistic scenarios. Unfortunately, the IGBT wafer/die cannot be tested in DCs before packaging/assembly.

In recent years, with the remarkable development of smart sensors, the traditional sensing techniques have changed dramatically. Pagani *et al.* proposed world's first contactless sensing system named ElectroMagnetic Wafer Sort (EMWS) for radio-frequency identification (RFID) wafer testing [24]. EMWS delivers power and communicates with the RFID antenna chips through electromagnetic (EM) waves. The test pads on dies can be removed; it enables significant miniaturization of the RFID chips. This EM -based sensing technique enhances the quality and reliability of low-power RF circuits with the advantage of contactless. This benefit enables high testing parallelism, and it reduces the test cycle and increases yield with high-throughput capability.

According to the technologies and research works mentioned above, it can be inferred that EM sensing is a possible technique that can be used to overcome the challenges that the conventional methods have failed to demonstrate. However, the EMWS system is only capable for testing low-power circuits. Hence, it is valuable to investigate a new and smart sensing technique for both inspection and testing of high-power semiconductor materials and capable of high-throughput capability. Thanks to the emerging internet of things-based sensing techniques, real-time fault diagnosis, and monitoring becoming a more realistic method for inspecting the industrial applications [25]–[27], there are up to 600 processes in semiconductor device manufacturing; the technique is even more important in the semiconductor industries. Here we propose an AR-aided smart sensing system for in-line condition monitoring of IGBT wafers. A series of signal processing algorithms are applied for enabling sensor intelligence. Based on infrared–visible fusion (IVF) in EM thermography, an in-time supplementary palpable three-dimensional (3-D) thermography layer is integrated with an IGBT wafer in real-world environment. Although the automation of wafer sensing systems has been a growing emphasis during the past decade, the fabs are still strongly dependent on experienced operators and engineers; the human fatigue and mistakes are always an important issue that affects yield [28]. AR technology can dramatically enhance the perception and interaction between operators and industrial systems as well as the surrounding world. The rest of this paper is organized as follows. The physical principle of the sensor system and the proposed methods are introduced in Section II. IGBT wafer inspection and the testing result are shown in Section III. IVF and AR are demonstrated in Section IV. The conclusion is examined in Section V.

II. Principle of the Smart Sensing System

To empower the sensors intelligently, a series of signal processing algorithms are applied to output the required sensing results. The theoretical background of the EM thermography sensing system is introduced. In order to characterize the inside property of IGBT dies, one of independent component analysis (ICA) is applied for investigation.

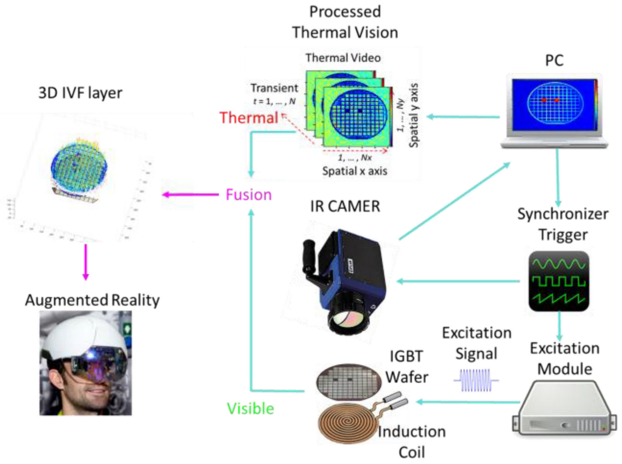

Fig. 2. Proposed AR-aided smart sensing system.

A. EM Thermography

The EM thermography system diagram is illustrated as a part in Fig. 2. A pulse signal from the function generator triggers infrared (IR) camera both to start recording the thermal video and simultaneously switch ON the induction heater to introduce inductive heating in the semiconductor wafer. Normally, the thermal videos are recorded for 1 s, which includes two stages, 200 ms for induction heating and 800 ms for cooling. The recorded thermal video is then transmitted to a PC for visualization and postprocessing, including defect identification and electrical/thermal property evaluation.

In general, high excitation frequencies will lead to a high thermal contrast (or high-temperature rise). The time-domain information will allow the derivation of defect profile information. The system has a quoted rise time (from the start of the heating period to full power) of 5 ms, which was verified experimentally. Water cooling of the coil is implemented to counteract direct heating of the coil. The SC7000sc is a FLIR IR camera and has an actively cooled detector with a maximum frame size of 640 × 512 on a 1.5–5.1 μm InSb detector. The camera has a sensitivity of <25 mK and a maximum full frame rate of 383 Hz. With the option to increase the frame rate with windowing of the image, the frame rate is set as 1000 Hz in the experiments.

When an alternating EM field is excited and interacts with an electrically conducting object, an eddy current is induced inside and flows through the conductor. The energy dissipated in the material is converted into heat. This is the process of induction heating or Joule heating. According to Joule's first law

$$Q = I^2 \cdot R_e \cdot t \tag{1}$$

where Q is the amount of induction heat, I is current, R_e is the amount of electric resistance present in the material, and t is the amount of time of the heating process. The relation of current density and electric field is

$$J = \sigma \cdot E \tag{2}$$

$$E = \rho_r \cdot J. \tag{3}$$

Equations (2) and (3) are substituted into (1) to obtain the following equation:

$$Q_e = \frac{1}{\sigma}|J|^2 = \frac{1}{\sigma}|\sigma \cdot E|^2 \tag{4}$$

where $\rho_r = 1/\sigma$ is the resistivity; this directly resembles (1). We can see that the local electrical conductivity σ of the DUTs is the key parameter, which determines the local EM heating when the excited EM field is uniform across the sample surface. According to the energy conservation and Fourier's law of heat conduction, the EM heat source term Q_e in the heat equation implemented by

$$Q_e = \rho \cdot C_p \frac{\partial T}{\partial t} + \nabla \cdot q \tag{5}$$

$$q = -k \cdot \nabla T \tag{6}$$

where ρ is the solid density of DUTs, C_p is the solid heat capacity at constant pressure, k is the solid thermal conductivity, and it describes the relationship between the heat flux vector q and the temperature gradient ∇T, which is Fourier's law of conduction. Finally, we can have the inductive heating by substituting (6) into (5)

$$Q_e = \rho \cdot C_p \frac{\partial T}{\partial t} - \nabla \cdot (k \cdot \nabla T). \tag{7}$$

The subsurface gate runner metallization is the main defect mechanism of the IGBT wafer under test in this paper. As (4) indicates that the electrical conductivity of the material plays a very important role in induction heating. Like most of the other thermography-based nondestructive testing and evaluation (NDT&E) techniques, EM thermography identifies and localizes defects by searching the "hot/cool spots" in the thermal patterns. The aim of utilizing the IR thermal camera in this case is not to measure the temperature, but to extract the contrast in the thermal map to evaluate the abnormal thermal responses generated by the defects. Based on these two points, the induction heating is stronger at defect locations due to eddy current concentration, which is affected by the variations in local electrical conductivity. This would provide high contrast between defects and nondefective areas in thermal maps. As shown in (7), the thermal conductivity influences the thermal information captured by the camera, especially in the heat diffusion stage, which resulted in different temperature profiles in the thermal pattern. More detailed information can be found in [29].

Based on the above considerations, the induction heating provides a unique advantage than other heating methods in this case, which is it mainly induces heating in metal layers rather than silicon materials, and the defects we are interested in mainly exist in the metal layers.

B. Independent Component Analysis

To illustrate the thermal responses in different layers, the ICA method is used for separating and visualizing hidden defects in thermography. As one of ICA methods, the multichannel morphological component analysis (MMCA) has been widely used in thermography applications. In this paper, it is applied to deal with the sparse and independence property of the IGBT wafer.

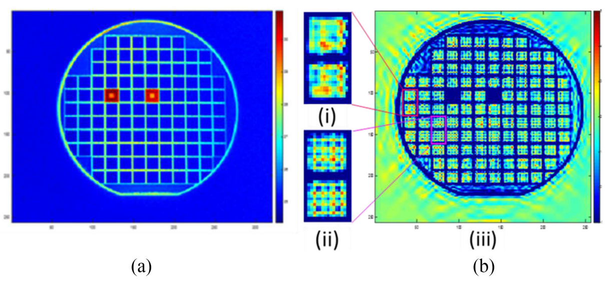

Fig. 3. IR images of IGBT wafer. (a) Raw data from the IR camera. (b) Wafermap of subsurface defects.

The technique is used for detecting and separating the influences of different layers and their combined information in IR images. Because of different transient thermal behaviors exist, as discussed in Section II-A, the inside multilayer structures of IGBT dies in the wafer can be identified and separated by calculating the cross-correlation of the estimated mixing vectors. MMCA learning algorithm searches for the linear transformation to make the components statistically independent to achieve the separation of the different layers in the IGBT structure. The advantage of the sparse representation of multichannel data in large overcomplete dictionaries to separate features in the data based on their morphology makes it capable to detect abnormal inside the IGBT dies. Because the amount of informational data at the target area is very small compared to the whole IR image, the defects in IGBT dies meet the sparse property criterion very well. The measurement $\mathbf{I}_M$ can be written as a multiplying of estimated decorrelation matrix $\mathbf{X}_{\mathrm{MMCA}}$ and mixing matrix $\mathbf{M}_{\mathrm{MMCA}}$ plus noise

$$\mathbf{I}_M = \mathbf{M}_{\mathrm{MMCA}}\mathbf{X}_{\mathrm{MMCA}} + \mathbf{N}_{\mathrm{noice}}. \tag{8}$$

The row vectors of $\mathbf{I}_M$, $\mathbf{X}_{\mathrm{MMCA}}$, and $\mathbf{M}_{\mathrm{MMCA}}$ are $\mathbf{i}_p$, $\mathbf{x}_p$, and $\mathbf{m}_p$ ($p = 1, \ldots, P$), respectively. Each $\mathbf{x}_p$ can be described as $\mathbf{x}_p^T = \mathbf{\Phi}_p \mathbf{a}_p$ with an overcomplete dictionary $\mathbf{\Phi}_p$ and a sparse representation $\mathbf{a}_p$.

The estimation of and $\mathbf{M}_{\mathrm{MMCA}}$ is governed by the following equation [30]:

$$\begin{aligned}\{\hat{\mathbf{M}}_{\mathrm{MMCA}}, \hat{\mathbf{X}}_{\mathrm{MMCA}}\} &= \arg\min_{\mathbf{M}_{\mathrm{MMCA}}, \mathbf{X}_{\mathrm{MMCA}}} \|\mathbf{I}'_M - \mathbf{M}_{\mathrm{MMCA}}\mathbf{X}_{\mathrm{MMCA}}\|^2_{\mathrm{Fro}} \\ &\quad + \sum_p \lambda_p \left\|\mathbf{x}_p \mathbf{\Phi}_p^+\right\|_1 \end{aligned} \tag{9}$$

where $\|\mathbf{M}\|^2_{\mathrm{Fro}} = \mathrm{trace}(\mathbf{M}^T\mathbf{M})$, here "Fro" denotes the Frobenius norm. $\mathbf{\Phi}_p^+$ is the updated $\mathbf{\Phi}_p$ in the next iteration; λ_p denotes the sparse parameters and $\|\mathbf{x}_p\mathbf{\Phi}_p^+\|_1$ forms the L1-norm regularization. From (9), by minimizing the objective function with respect to $\mathbf{x}_p$ when $\mathbf{m}_p$ is fixed, it can be derived as

$$\begin{aligned}\mathbf{x}_p &= \frac{1}{\|\mathbf{m}_p\|_2^2}[\mathbf{m}_p^T\mathbf{I}_m - \frac{\lambda_p}{2}\mathrm{sign}(\mathbf{x}_p\mathbf{\Phi}_p^+)\mathbf{\Phi}_p^{+T} \\ \mathbf{m}_p &= \frac{1}{\|\mathbf{m}_p\|_2^2}\mathbf{I}_m\mathbf{x}_p^T\end{aligned} \tag{10}$$

where $\mathbf{I}_m = \mathbf{I}_M - \sum_{p' \neq p} \mathbf{m}_{p'}\mathbf{x}_{p'}$. The MMCA algorithm is presented in [31, Section II].

III. IGBT Wafer Inspection and Testing

The raw IR image of the IGBT wafer at the maximum heating transient is shown in Fig. 3(a). Fig. 3(b) shows the thermal pattern of IGBT wafer after applying the MMCA algorithm introduced in Section II-B. It revealed the inside defects of IGBT semiconductor wafer, as shown in Fig. 3(iii). International Rectifier manufactured the IGBT wafer used in this paper. The wafer model is IRGC75B120KB; static electrical testing has been conducted after being manufactured.

As seen from the visible image of IGBT wafer shown in Fig. 1, black ink dots are marked on the defective IGBT dies. The unqualified parameter of this wafer is the $V_{\mathrm{CE(ON)}}/V_{\mathrm{CEsat}}$, I_{CES}, and I_{GES}, which means the defective dies are suffered from inside mechanical failures. The mesh geometry of the IGBT dies shows metallization layer of the gate runners. A gate runner structure in defect-free IGBT die is shown in Fig. 3(i): the two health IGBT dies show a clear and tidy mesh pattern. The higher temperature shown in the intact mesh represents the cross-sectional area of the metal via; the gate runner via shows slightly lower temperature response, and low-temperature response areas are the emitter of the IGBT, which have no induction heating generated on them. Fig. 3(ii) shows two defective IGBT dies, which are identified by the electrical probe sensing. The mesh geometry is destructed, vast areas of hot spots are illustrated, which may indicate that the isolation layers are failed due to mechanical defects inside the dies. The destructed mesh structures are found in all the defective IGBT dies identified by the static electrical testing. To compare with the traditional electrical probing, as shown in Fig. 1, the I_{GES} results of Fig. 3(ii) are 3.16E–07A and 2.59E–07A, and 3.30E–09A and 4.15E–09A are for Fig. 3(i). It shows that the I_{GES} presents much higher values of the defective dies than those of health dies that are identified by the method proposed in this paper. The test condition is V_{GE} at 30 V; the failure criterion is set to 50 nA. All the ink-marked dies shown in Fig. 1 have different degrees of blurred mesh pattern and large areas of hot spots. Moreover, some of the qualified IGBT dies that passed the electrical testing also illustrate slight destructive and blurry mesh pattern in the thermal image. There are three possible reasons for this phenomenon. The first one is that all the power electronic devices have quite considerable electrical redundancy. For example, the IGBT wafer used in this paper shows the minimum V_{CES} is 1200 V in the datasheet, and the customers employed it at or less than 1200 V, but normally, it can survive at least 1400 V of V_{CES}. The IGBT dies passed electrical testing and show that defective areas in the thermal image can survive for 1200 V V_{CES}, but may not have much more redundancy than other defects free dies. The second reason is that those dies showed qualified static electrical parameters but may fail in dynamic electrical testing after they are assembled. Finally, even the dies can be qualified by both SCs and DCs testing; the dies may tend to be fatigued easier and severe than the defect-free dies.

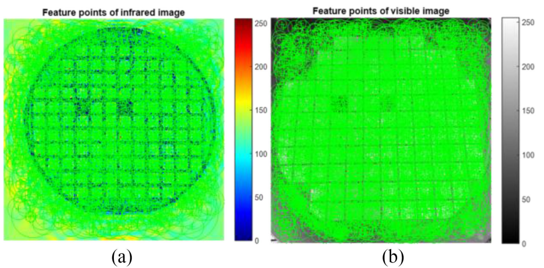

Fig. 4. Feature points researching and corresponding. (a) Feature points of the IR image. (b) Feature points of the visible image.

The test results show that the EM thermography is very effective for chip characterization. Since the technique employed both electrical and IR thermal information for sensing material property changes, in these two testing conditions, it demonstrates better sensitivities than traditional sensing technologies.

IV. Infrared–Visible Fusion and Augmented Reality

AR is a technique that layers computer-generated sensory input atop an existing reality to make it more informative through the ability to interact with it. Here, the EM thermography of the wafer inside defects is supplemented to a live direct view of operators or engineers who perform the inspection and testing of IGBT wafers. In this case, the augmentation is more attractive since the IR image can provide invisible but important information of DUT properties. To achieve the AR function of in-line condition monitoring of IGBT wafers, a palpable 3-D thermographic layer needs to be generated and overplayed to the existed surrounding environment. Since the operators need to inspect both IR information and the visible objects, it requires the view of the physical environment and targets with high-level accuracy and precision. The most important measure of an AR system is the integration of the augmentations with the real world. Based on the precise correspondence between the IR images and visible images, IVF can be implemented. Then the fused sensory output is integrated into the point cloud to transform into the 3-D layer. It can significantly improve the perception of the IGBT semiconductor wafer inspectors and further to improve the efficiency and the inspection throughput. The speeded-up robust-features (SURF) [32] is a robust local feature detector and descriptor for a different vison-based application; it uses the integral images for image convolutions to sharply reduce the number of operations for image convolutions. In machine vision, it is mainly used for image registration and 3-D reconstruction. To achieve precise IVF, the scale- and rotation-invariant detector and descriptor, SURF is applied for finding corresponding points between the IR image and visible image of the IGBT wafer. Fig. 4 shows the feature points detected in the IR image and visible image respectively. It takes around 5.4 s for feature matching between thermal and visible images both with 256 $\times$ 256 pixels in MATLAB using SURF, on a Windows computer with Intel Core i7-7500U CPU.

The SURF interest point detector detects that those points have the scale and location information of feature points, and then generate local descriptor using SURF method and global

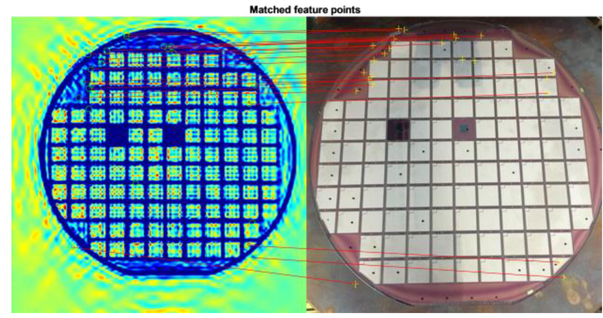

Fig. 5. Feature corresponding between the IR image and visible image.

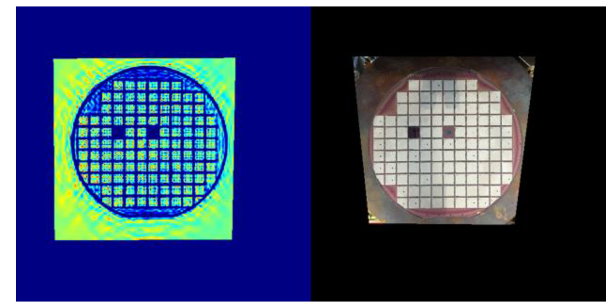

Fig. 6. Affine mapping for IR and visible images.

descriptor from the edge image. The two descriptors are combined with weightings to form the final descriptor for each interest point. The final descriptor is applied to the two images and they are matched by their pairwise Euclidean distance. The initial matching is refined with the random sample consensus algorithm to get the final matching [33]–[36]. Those feature points, which can be corresponded to each other or matched to the feature descriptor properties, are corresponded and shown in Fig. 5.

A total of 24 corresponding points have been detected and matched to each other, shown as the green circles in the IR image and the yellow stars in the visible image. Actually, only four matched feature points would be enough for the IVF. In this case, with many more mathced pairs, the precise fusion corresponding can be guaranteed. With 24 matched feature points detected, the transfer matrix generated can highly fit to the affine transformation for the image mapping. Fig. 6 shows the mapping result after affine transformation. In this technique, an initial affine transform matrix is formed by randomly choosing several matched pairs. Then other matched pairs which fit with the matrix are used to iteratively refine it. After the image mapping, the scale and orientation of both IR and visible images exactly correspond. Considering it to be reader-friendly, the IVF is performed in a simple background; we have applied a mask to cut the IGBT wafer from both IR and visible images, as shown in Fig. 7. In the realistic scenario of IGBT wafer inspection, the mask for the visible image is unnecessary since the AR elements would only be the thermal layer, which is limited to the wafer area. The IVF image using this match result is shown in Fig. 8. Both visible information and thermal information are presented in it which is generated using the wavelet fusion

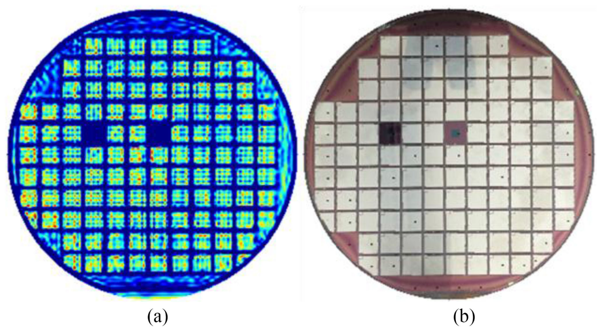

Fig. 7. IGBT wafer images. (a) IR image. (b) Visible image.

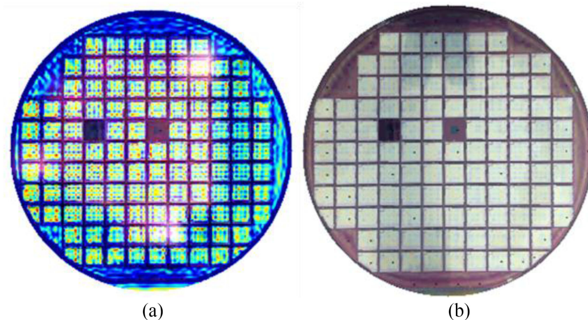

Fig. 8. IVF with different ratio. (a) 9:1. (b) 1:9.

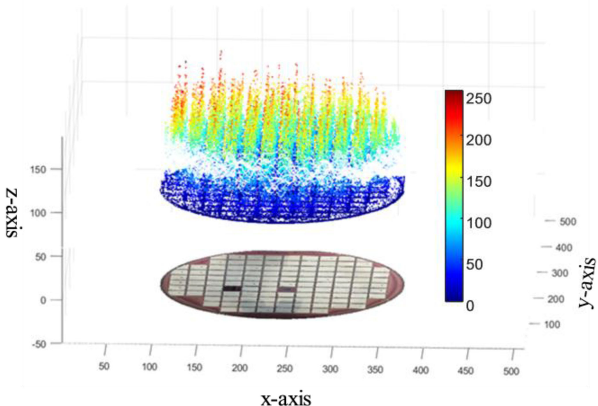

Fig. 9. 3-D IR image integrated in point cloud overplayed on the visible image.

algorithm [37]. In detail, the final matching is used to estimate the transform matrix from one image to another, finally merging them with wavelet decompositions at level 5 using Symlets 4 wavelet (sym4) by taking the maximum of absolute value of the coefficients [36]. The ratio of IVF can be adjusted from 0 to 10 based on the inspecting application. Fig. 8(a) shows that the ratio of IVF is 9:1 and Fig. 8(b) is 1:9. In the real application, the operators can adjust the ratio in-time to meet the best perception requirement.

Since the fusion results are not intuitive, to achieve a better AR effect, a 3-D layer of thermographic is overlaid on the visible image of the IGBT wafer, as shown in Fig. 9. Both IR and visible images are embedded into the point cloud to build the 3-D model of IVF. The actual IGBT wafer samples are static on the inspection bench or the wafer handler in the realistic scenario, the variable in AR processing is the position of the inspector. With the previous image registration and correspondence, the scale and orientation of the augmented 3-D thermal layer can be adjusted to fit the operator vision field in the live direct view. Any point in Fig. 9 is scanned and registered in the point cloud; the x-, y-, and z-axis indicate the position of the IR–visible-fused pixels. For the purpose of illustration, the distance between the IR image and visible image are separated for 100 pixels in the point cloud. However, in the realistic scenario, the two images are stacked together and the 3-D IR information is overlapped and highlighted above the visible image. Hence, the thermal pattern is illustrated in a tomographic way; the defects can be easily identified and graded by the inspectors.

In the AR image, the defects are highlighted with a higher thermal response, and the locations are corresponded in the visible image. Different levels of the defects can be directly presented by adjusting the criteria of the quality requirement. In this case, the chip channels and the calibration chips are separated from the defects information, as shown in Fig. 9. Based on the preimage processing steps shown in Figs. 4–8, the different layers precisely correspond to each other; the AR image generated in the final stage can be illustrated from different angles to meet the visualization requirements of the operators. With the aid of the AR visualization, the efficiency of the wafer testing could be significantly improved and the throughput of the wafer manufacture ability could be realized considerably.

V. Conclusion

In this paper, an AR-aided smart sensing system for in-line condition monitoring of IGBT wafers was proposed and investigated. The IVF was performed and embedded into the 3-D point that could generate a 3-D layer sensory augmented element atop of the reality environment. The process of the AR-IVF-aided IGBT inspection can be summarized as follows:

1) acquiring the visible image of IGBT wafer;
2) acquiring IR thermal image of IGBT wafer under inductive heating;
3) processing thermal image to reveal subsurface defects of IGBT wafer;
4) featuring mapping between thermal and visible images;
5) performing IVF with different scales depending on the operator requirement;
6) embedding fused thermal features into the point cloud to build the 3-D model and project the 3-D layer on the visible layer of the IGBT wafer.

After a series of imaging processing and feature extracting, the AR-aided IGBT wafer inspection system was constructed.

Compared to the traditional low-throughput sensing technologies, the proposed AR-aided smart sensing system can perform the inspection of IGBT wafer on the time scale within 1 s in an ideal condition. This rapid inspection capability enables the in-line condition monitoring for the IGBT wafers in the fabs. Currently, the AR-based IVF inspection technique for IGBT wafer is just proposed and is in an infant stage. It cannot replace the popular electrical tests at this moment for sure, but it can be an assisting method for complementary or secondary inspections to improve the yield management. As described in this

paper, the subsurface defects were investigated. With a deeper investigation and research in this technique, the optimized systems in the future may inspect more types of other defects such as pinholes and dislocations in semiconductor wafers.

Acknowledgment

The authors would like to thank S. Ding for her support during the research project.

References

[1] J. Ebrahimi, E. Babaei, and G. B. Gharehpetian, "A new multilevel converter topology with reduced number of power electronic components," *IEEE Trans. Ind. Electron.*, vol. 59, no. 2, pp. 655–667, Feb. 2012.

[2] A. Myaing and V. Dinavahi, "FPGA-based real-time emulation of power electronic systems with detailed representation of device characteristics," *IEEE Trans. Ind. Electron.*, vol. 58, no. 1, pp. 358–368, Jan. 2011.

[3] V. Smet *et al.*, "Ageing and failure modes of IGBT modules in high-temperature power cycling," *IEEE Trans. Ind. Electron.*, vol. 58, no. 10, pp. 4931–4941, Oct. 2011.

[4] Y. Tsuruta, Y. Ito, and A. Kawamura, "Snubber-assisted zero-voltage and zero-current transition bilateral buck and boost chopper for EV drive application and test evaluation at 25 kW," *IEEE Trans. Ind. Electron.*, vol. 56, no. 1, pp. 4–11, Jan. 2009.

[5] A. Froggatt and M. Schneider, "Nuclear power versus renewable energy—A trend analysis [Point of View]," *Proc. IEEE*, vol. 103, no. 4, pp. 487–490, Apr. 2015.

[6] M. P. Fanti, W. Ukovich, and R. Uzsoy, "Guest Editorial Special Section on emerging advances in logistics systems: Integrating remote sensing, IT, and autonomy," *IEEE Trans. Autom. Sci. Eng.*, vol. 13, no. 4, pp. 1420–1421, Oct. 2016.

[7] Y. Hou and J. Zhong, "Challenges ahead: Currents status and future prospects for Chinese energy," *IEEE Power Energy Mag.*, vol. 10, no. 3, pp. 38–47, May-Jun. 2012.

[8] M. Freed, M. Kruger, C. J. Spanos, and K. Poolla, "Autonomous on-wafer sensors for process modeling, diagnosis, and control," *IEEE Trans. Semicond. Manuf.*, vol. 14, no. 3, pp. 255–264, Aug. 2001.

[9] T. Rim *et al.*, "Electrical characteristics of doped silicon nanowire channel field-effect transistor biosensors," *IEEE Sensors J.*, vol. 17, no. 3, pp. 667–673, Feb. 2017.

[10] H. Lee, Y. Kim, and C. O. Kim, "A deep learning model for robust wafer fault monitoring with sensor measurement noise," *IEEE Trans. Semicond. Manuf.*, vol. 30, no. 1, pp. 23–31, Feb. 2017.

[11] M. Koyanagi, T. Fukushima, and T. Tanaka, "High-density through silicon vias for 3-D LSIs," *Proc. IEEE*, vol. 97, no. 1, pp. 49–59, Jan. 2009.

[12] H. Cheng, H. Chen, and B. W. Mooring, "Accuracy analysis of dynamic-wafer-handling robotic system in semiconductor manufacturing," *IEEE Trans. Ind. Electron.*, vol. 61, no. 3, pp. 1402–1410, Mar. 2014.

[13] D. Tsai, I. Chiang, and Y. Tsai, "A shift-tolerant dissimilarity measure for surface defect detection," *IEEE Trans. Ind. Informat.*, vol. 8, no. 1, pp. 128–137, Feb. 2012.

[14] E. Bitincka, G. Gilardi, and M. K. Smit, "On-wafer optical loss measurements using ring resonators with integrated sources and detectors," *IEEE Photon. J.*, vol. 6, no. 5, pp. 1–12, Oct. 2014, Art no. 6601212.

[15] D. Tsai and J. Luo, "Mean shift-based defect detection in multicrystalline solar wafer surfaces," *IEEE Trans. Ind. Informat.*, vol. 7, no. 1, pp. 125–135, Feb. 2011.

[16] M. Freed, M. Kruger, C. J. Spanos, and K. Poolla, "Autonomous on-wafer sensors for process modeling, diagnosis, and control," *IEEE Trans. Semicond. Manuf.*, vol. 14, no. 3, pp. 255–264, Aug. 2001.

[17] J. Li *et al.*, "An electromechanical model and simulation for test process of the wafer probe," *IEEE Trans. Ind. Electron.*, vol. 64, no. 2, pp. 1284–1291, Feb. 2017.

[18] E. F. Scarselli, L. Perilli, L. Perugini, and R. Canegallo, "A 40 nm CMOS I/O Pad design with embedded capacitive coupling receiver for non-contact wafer probe test," *IEEE Trans. Circuits Syst. I: Regular Papers*, vol. 62, no. 7, pp. 1737–1746, Jul. 2015.

[19] Y. Liu, T. Luk, and S. Irving, "Parameter modeling for wafer probe test," *IEEE Trans. Electron. Packag. Manuf.*, vol. 32, no. 2, pp. 81–88, Apr. 2009.

[20] K. R. Skinner *et al.*, "Multivariate statistical methods for modeling and analysis of wafer probe test data," *IEEE Trans. Semicond. Manuf.*, vol. 15, no. 4, pp. 523–530, Nov. 2002.

[21] B. Tunaboylu, "Power delivery performance of probe test systems for semiconductor wafers," *IEEE Design Test*, vol. 33, no. 6, pp. 72–76, Dec. 2016.

[22] J. E. Cotter, J. H. Guo, P. J. Cousins, M. D. Abbott, F. W. Chen, and K. C. Fisher, "P-type versus n-type silicon wafers: Prospects for high-efficiency commercial silicon solar cells," *IEEE Trans. Electron Devices*, vol. 53, no. 8, pp. 1893–1901, Aug. 2006.

[23] E. Simoen, G. Eneman, P. Verheyen, R. Loo, K. De Meyer, and C. Claeys, "Processing aspects in the low-frequency noise of nMOSFETs on strained-silicon substrates," *IEEE Trans. Electron Devices*, vol. 53, no. 5, pp. 1039–1047, May 2006.

[24] A. Pagani, A. Finocchiaro, and G. Girlando, "Electronic device for electromagnetic expansion and concentration," U.S. Patent Appl., US20140347244 A1, Nov. 27, 2014.

[25] B. Akin, S. Choi, U. Orguner, and H. A. Toliyat, "A simple real-time fault signature monitoring tool for motor-drive-embedded fault diagnosis systems," *IEEE Trans. Ind. Electron.*, vol. 58, no. 5, pp. 1990–2001, May 2011.

[26] C. Shang, F. Yang, B. Huang, and D. Huang, "Recursive slow feature analysis for adaptive monitoring of industrial processes," *IEEE Trans. Ind. Electron.*, vol. 65, no. 11, pp. 8895–8905, Nov. 2018.

[27] D. Binu and B. S. Kariyappa, "A survey on fault diagnosis of analog circuits: Taxonomy and state of the art," *AEU - Int. J. Electron. Commun.*, vol. 73, pp. 68–83, Mar. 2017.

[28] M. Wang and C. Huang, "Evaluating the eye fatigue problem in wafer inspection," *IEEE Trans. Semicond. Manuf.*, vol. 17, no. 3, pp. 444–447, Aug. 2004.

[29] K. Li, G. Y. Tian, L. Cheng, A. Yin, W. Cao, and S. Crichton, "State detection of bond wires in IGBT modules using eddy current pulsed thermography," *IEEE Trans. Power Electron.*, vol. 29, no. 9, pp. 5000–5009, Sep. 2014.

[30] L. Cheng, B. Gao, G. Y. Tian, W. L. Woo, and G. Berthiau, "Impact damage detection and identification using eddy current pulsed thermography through integration of PCA and ICA," *IEEE Sensors J.*, vol. 14, no. 5, pp. 1655–1663, May 2014.

[31] J. Bobin, Y. Moudden, J. Starck, and M. Elad, "Morphological diversity and source separation," *IEEE Signal Process. Lett.*, vol. 13, no. 7, pp. 409–412, Jul. 2006.

[32] H. Bay, A. Ess, T. Tuytelaars, and L. Gool, "Speed-up robust features (SURF)," *Comput. Vis. Image Understand.*, vol. 110, pp. 346–359, Jun. 2008.

[33] Z. Hossein-Nejad and M. Nasri, "An adaptive image registration method based on SIFT features and RANSAC transform," *Comput. Elect. Eng.*, vol. 62, pp. 524–537, 2017.

[34] M. Saval-Calvo, J. Azorin-Lopez, A. Fuster-Guillo, and J. Garcia-Rodriguez, "Three-dimensional planar model estimation using multi-constraint knowledge based on k-means and RANSAC," *Appl. Soft Comput*, vol. 34, pp. 572–586, 2015.

[35] X. Wu, Q. Zhao, and W. Bu, "A SIFT-based contactless palmprint verification approach using iterative RANSAC and local palmprint descriptors," *Pattern Recognit*, vol. 47, no. 10, pp. 3314–3326, 2014.

[36] C. Tang, G. Y. Tian, X. Chen, J. Wu, K. Li, and H. Meng, "Infrared and visible images registration with adaptable local-global feature integration for rail inspection," *Infrared Physics Technol.*, vol. 87, pp. 31–39, 2017.

[37] G.Pajares and J. Cruz,"A wavelet-based image fusion tutorial," *Pattern Recognit.*, vol. 37, pp. 1855–1872, 2004.

Kongjing Li (M'13) received the B.Eng. degree in electronic engineering from the University of Hull, Hull, U.K., in 2010, the M.Sc. degree in electrical technology for sustainable and renewable energy systems from the University of Nottingham, Nottingham, U.K., in 2011, and the Ph.D. degree in electrical and electronic engineering from Newcastle University, Newcastle upon Tyne, U.K., in 2017.

Since April 2018, he has been a Senior Engineer with Dynex Semiconductor, Ltd., Lincoln, U.K. His research interests include reliability of power semiconductor devices, SiC power module designs, sensor technologies, thermography, and NDT&E techniques.

Gui Yun Tian (M'01–SM'03) received the B.Sc. degree in metrology and instrumentation and the M.Sc. degree in precision engineering from the University of Sichuan, Chengdu, China, in 1985 and 1988, respectively, and the Ph.D. degree in nondestructive testing from the University of Derby, Derby, U.K., in 1998.

From 2000 to 2006, he was a Lecturer, Senior Lecturer, Reader, Professor, and Head of the group of systems engineering with the University of Huddersfield, Huddersfield, U.K. Since 2007, he has been with Newcastle University, Newcastle upon Tyne, U.K, as a Chair Professor involved with sensor technologies. He is currently an Adjunct Professor with the School of Automation Engineering, University of Electronic Science and Technology of China, Chengdu. He has also coordinated several research projects from the Engineering and Physical Sciences Research Council, Royal Academy of Engineering, and FP7. He also has a good collaboration with leading industrial companies such as Airbus, Rolls Royce, BP, nPower, Network Rail, and TWI.

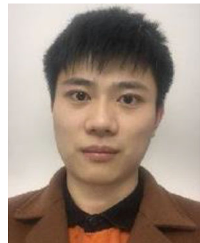

Xiaotian Chen received the B.Eng. degree in electrical and electronic engineering from the joint program between Nanjing Normal University, Nanjing, China, and Northumbria University, Newcastle upon Tyne, U.K., in 2014. He is currently working toward the Ph.D. degree in electrical and electronic engineering at Newcastle University.

His current research interests include three-dimensional reconstruction, thermal image processing, and nondestructive testing.

Chaoqing Tang received the B.Sc. degree in communication engineering from Southwest University, Chongqing, China, in 2015. He is currently working toward the Ph.D. degree in electrical and electrical engineering at Newcastle University, Newcastle Upon Tyne, U.K.

His research interests include compressed sensing, modeling, and performance analysis of wireless systems, physical layer security, electromagnetic nondestructive testing, and microwave imaging.

Haoze Luo (M'15) received the B.S. degree in electrical engineering and automation and the M.S. degree in power electronics and power drives from the Hefei University of Technology, Hefei, China, in 2008 and 2011, respectively, and the Ph.D. degree in power electronics and power drives from Zhejiang University, Hangzhou, China, in 2015.

He is currently a Postdoc with the Department of Energy Technology, Aalborg University, Aalborg, Denmark. From January to April 2015, he was a Visiting Researcher with Newcastle University, Newcastle upon Tyne, U.K. His research interests include high-power converters and reliability of high-power modules.

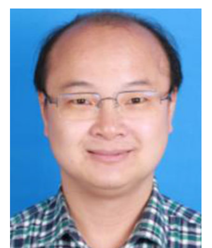

Wuhua Li (M'09) received the B.Sc. and Ph.D. degrees in power electronics and electrical engineering from Zhejiang University, Hangzhou, China, in 2002 and 2008, respectively.

From 2004 to 2005, he was a Research Intern, and from 2007 to 2008, a Research Assistant with GE Global Research Center, Shanghai, China. From 2008 to 2010, he joined the College of Electrical Engineering, Zhejiang University, as a Postdoctor. In 2010, he was promoted as an Associate Professor. Since 2013, he has been a Full Professor with Zhejiang University. From 2010 to 2011, he was a Ryerson University Postdoctoral Fellow with the Department of Electrical and Computer Engineering, Ryerson University, Toronto, ON, Canada. He has authored or coauthored more than 200 peer-reviewed technical papers and holds more than 30 issued/pending patents. His research interests include power devices, converter topologies, and advanced controls for high power energy conversion systems.

Bin Gao (M'12–SM'14) received the B.Sc. degree from Southwest Jiao Tong University, Chengdu, China, in 2005, and the M.Sc. and Ph.D. degrees from Newcastle University, Newcastle upon Tyne, U.K., in 2011, all in communications and signal processing.

He is currently a Professor with the School of Automation Engineering, University of Electronic Science and Technology of China, Chengdu, China.

Xiangning He (M'95–SM'96–F'10) received the B.Sc. and M.Sc. degrees from the Nanjing University of Aeronautics and Astronautics, Nanjing, China, in 1982 and 1985, respectively, and the Ph.D. degree from Zhejiang University, Hangzhou, China, in 1989, all in applied power electronics and electrical engineering.

From 1985 to 1986, he was an Assistant Engineer with the 608 Institute of Aeronautical Industrial General Company, Zhuzhou, China. From 1989 to 1991, he was a Lecturer with Zhejiang University. In 1991, he received a Fellowship from the Royal Society of U.K., and conducted research in the Department of Computing and Electrical Engineering, Heriot-Watt University, Edinburgh, U.K., as a Postdoctoral Research Fellow for two years. In 1994, he joined Zhejiang University as an Associate Professor. Since 1996, he has been a Full Professor with the College of Electrical Engineering, Zhejiang University. He was the Director of Power Electronics Research Institute, the Head of the Department of Applied Electronics, the Vice-Dean of the College of Electrical Engineering, and he is currently the Director of the National Specialty Laboratory for Power Electronics, Zhejiang University. His research interests include power electronics and their industrial applications.

Dr. He was an IEEE Distinguished Lecturer by the IEEE Power Electronics Society in 2011. He is a Fellow of the Institution of Engineering and Technology (formerly IEE), U.K.

Nick Wright received the bachelor's and Ph.D. degrees from Edinburgh University, Edinburgh, U.K.

He is currently a Professor of Electronic Materials with Newcastle University, Newcastle upon Tyne, U.K., and a Fellow of the Turing Institute. He has led major projects on power semiconductor devices, robotics, and AI. He has authored more than 200 papers, contributed to more than 10 patents, and made numerous conference presentations. His research interests include electronic materials, power devices, and the applications of materials to robotics and artificial intelligence—particularly for manufacturing and deep ocean exploration.